Migration and aggregation of fission products and their impacts on physical properties in UO_2: Deep potential molecular dynamics simulations

Zhihong Chen,[1] Yunfei Hong,[1] Junkai Deng,[1,*] Zhibin Gao,[1] Ronghua Chen,[2] Rui Tang,[3] Hongxing Xiao,[3,†] Xiangdong Ding,[1] and Jun Sun[1]

[1]State Key Laboratory for Mechanical Behavior of Materials, Xi'an Jiaotong University, Xi'an 710049, China
[2]School of Nuclear Science and Technology, Xi'an Jiaotong University, Shaanxi, Xi'an 710049, China
[3]National Key Laboratory of Nuclear Reactor Technology, Nuclear Power Institute of China, Chengdu 610213, China

(Received 10 January 2025; accepted 13 June 2025; published 7 August 2025)

Fission products (FP) are inevitable byproducts of nuclear fission in the fuel during reactor operation. The migration and aggregation of FP in uranium dioxide (UO_2)-based nuclear fuels play a crucial role in determining fuel performance and safety throughout the nuclear fuel cycle. However, accurately characterizing the atomic diffusion and early cluster formation of FP remains challenging in experiments. To address this issue, we employed self-developed deep potential (DP) models for UO_2-Xe and UO_2-I systems to perform molecular dynamics (MD) simulations. These simulations investigate the effects of Xe and I migration and aggregation on the mechanical properties and thermal conductivity of UO_2 fuel. First, the accuracy of the DP models was verified. Next, the diffusion coefficients and cluster formation behavior of Xe and I in UO_2 were analyzed, revealing three distinct temperature-dependent diffusion mechanisms. Furthermore, the MD simulation results demonstrate that the incorporation of FP significantly reduces the mechanical properties and thermal conductivity of UO_2. Interestingly, the aggregation of FP into clusters mitigates these reductions, improving both mechanical properties and thermal conductivity. Notably, the recovery of mechanical properties through Xe aggregation is quite limited, primarily due to the formation of larger Xe clusters. In contrast, Xe aggregation leads to a more substantial improvement in thermal conductivity compared to I aggregation, attributed to reduced phonon scattering resulting from the fewer residual dispersed Xe atoms in the UO_2 matrix. These insights are critical for improving reactor safety and extending operational lifespans through a better understanding of the migration and aggregation of FP.

DOI: 10.1103/f3kx-84sy

I. INTRODUCTION

The migration and aggregation of fission products (FP) in uranium dioxide (UO_2)-based nuclear fuels are critical to the performance and safety throughout the nuclear fuel cycle [1–3]. Among the volatile fission products, iodine (I) [4,5] has been identified as a major contributor to stress corrosion cracking of the Zircaloy cladding, leading to fuel failures during reactor operation [6–10]. The iodine can further decay into xenon (Xe) [11,12], another typical fission product with low solubility in the fuel matrix, forming fission gas bubbles. The migration and aggregation of these fission products not only affect the mechanical and thermal properties of the fuel but also cause fuel swelling, potentially resulting in fuel element failure [13,14]. Therefore, a comprehensive understanding of the microstructural evolution caused by the migration and aggregation of FP, such as iodine and xenon, and their effects on the physical properties of nuclear fuel are highly desirable.

Numerous experimental studies have been conducted to enhance the understanding of FP behavior and improve predictions of microstructural evolution during reactor operation [15–19]. While in-pile data are essential for investigating FP behavior, they are often limited by an incomplete understanding of the entire physical process. Advanced techniques, such as in-situ ion irradiation using transmission electron microscopy (TEM), enable continuous observation of cluster growth and provide data on number density and size distribution [20]. Despite these advancements, accurately characterizing the nucleation process and the early growth stages of FP clusters remains challenging due to the inherent resolution limits of TEM equipment [21]. Furthermore, FP atoms are expected to form clusters much faster than grain boundary migration, complicating experimental measurements of transient cluster growth and associated changes in physical properties [21]. To address these challenges, molecular dynamics (MD) simulations offer a powerful complementary tool for studying FP evolution and its subsequent impact on the mechanical and thermal properties of nuclear fuel.

Theoretical and modeling approaches to study radiation damage have a history spanning over half a century. Given the large system size required to study FP migration and aggregation, MD simulations with empirical interatomic potentials have been particularly effective for investigating the interaction of radiation-produced defects in the fuel matrix [22,23]. As the dominant volatile fission product, Xe behavior

*Contact author: junkai.deng@mail.xjtu.edu.cn
†Contact author: xiaohongxing2003@163.com

in UO_2 has been extensively investigated by MD simulations, including diffusion mechanisms, Xe cluster nucleation, and the effect of Xe clusters on thermal conductivity [24–26]. However, comprehensive studies on the impact of Xe cluster dynamic nucleation and growth on the mechanical and thermal properties of UO_2 fuel remain scarce. Additionally, investigating iodine, the precursor to Xe, is crucial despite its lower concentration in nuclear fuels. Comparative studies of the Xe and I behavior in fuel are also of great interest, yet no empirical interatomic potential for I in UO_2 has been developed to date.

In this study, we developed two deep potential (DP) models (DP_{U-O-Xe} model and DP_{U-O-I} model) for UO_2-Xe and UO_2-I systems using a consistent strategy for investigating FP (Xe and I) diffusion, cluster formation, and growth. The accuracy of the trained DP models was validated by successfully reproducing DFT predictions over a broader configuration space. Employing MD simulations with validated DP models, we calculated the diffusion coefficients of Xe and I as a function of temperature at a specific FP concentration. Extensive MD simulations were conducted to analyze FP aggregation under different relaxation times. By evaluating the effects of microstructural evolution on the mechanical properties and thermal conductivity of UO_2 fuel, we provide new insights into the role of FP in determining the physical properties of nuclear fuel.

II. COMPUTATIONAL METHODS

A. Machine-learning interatomic potential

The DeePMD-kit package [27] enables the construction of deep learning-based representations of potential energy surfaces. The DP models, which dynamically embed configurations into descriptors using neural networks [28], have delivered DFT-level accuracy across diverse research fields [29–32], including finite molecules, extended systems, metallic systems, and chemically bonded systems [33]. However, the application of the DP model in nuclear fuel research is still in its infancy.

In the present work, the DP models for UO_2-Xe and UO_2-I systems were trained. The descriptors characterize the local environment of each atom within a cutoff radius R_c, which is set to 11 Å in this study. A smoothed version of the DP model is utilized to eliminate the discontinuity caused by the cutoff radius, with the inner cutoff value set to 10 Å. The p_ε, p_f, and p_ξ are the weight coefficients corresponding to the energy, force, and virial tensor, respectively. During the training procedure, p_ε increases from 0.02 to 2, while p_f decreases from 1000 to 1, and $p_\xi = 0$ increases from 0.02 to 1.

B. Generation of the training dataset and exploration protocol

To efficiently cover the relevant phase space, the DP generator (DP-GEN) [34] was employed to produce the configurations for training the DP model. The DP-GEN program integrates training, exploration, and labeling in a concurrent learning framework, iteratively refining the model until the desired accuracy is achieved.

The initial dataset for training the DP models included 1200 randomly distributed configurations generated using *ab initio* molecular dynamics (AIMD) simulations. First-principle calculations were performed within the framework of density functional theory (DFT), as implemented in the Vienna *ab initio* simulation package (VASP) [35,36]. The projector augmented-wave (PAW) method [37,38] was employed to treat the core and valence electrons. The Perdew-Burke-Ernzerhof (PBE) exchange-correlation functional of generalized gradient approximation (GGA) was adopted to treat the electron exchange and approximation [39]. An energy cutoff of 400 eV, a Gaussian smearing of 0.1 eV, and a k-point meshing of $1 \times 1 \times 1$ were used for all the calculations. To build ternary systems, Xe/I atoms were doped into octahedral interstitial sites of UO_2 supercells ($2 \times 2 \times 2$ unit cells with 96 atoms). The dataset was derived from fully relaxed AIMD trajectories sampled from an NVT ensemble. Two sets of DP-GEN workflows were conducted across a temperature range of 50 to 1800 K, corresponding to the UO_2-Xe and UO_2-I systems. In total, over 60000 configurations were labeled, constructing the training dataset.

C. MD simulations

The optimized DP models were employed to conduct MD simulations with periodic boundary conditions, utilizing the LAMMPS software package [40]. The time step was set as 1 femtosecond (fs) for all MD simulations, with temperature and pressure controlled via the Nosé-Hoover thermostat and barostat [41,42]. Visualization of atomic configurations was performed by using the Open Visualization Tool (OVITO) software [43].

To investigate atomic diffusion, a large supercell ($12 \times 12 \times 12$ with over 20000 atoms) was used to minimize size effects and statistical variation. Xe or I atoms were introduced into the UO_2 lattice by substituting 10% of uranium (U) atoms, with a corresponding number of oxygen (O) atoms removed to maintain charge neutrality, while abundant vacancies were introduced to mediate the diffusion of FP atoms. We used high FP concentrations to accelerate nucleation and growth, enabling statistically meaningful results within nanoscale simulations. High FP concentrations can also be regarded as the pre-nucleation stage of FP atoms forming bubbles in real situations, where the local FP concentration is significantly higher than in surrounding regions. Simulations were run for 80 picoseconds (ps) in the NPT ensemble at temperature intervals of 100K between 300 K and 1700 K.

Elastic constants are calculated using the stress-strain relationship, where small strains (ε) were applied to the lattice, and the resulting changes in total energy were analyzed. For cubic lattices like UO_2, only three independent nonzero elastic constants, C_{11}, C_{12} and C_{44}, were required. These were determined by Taylor expansion and expressed in Voigt notation as follows:

$$E_{tot}(V, \varepsilon_m) = E_{\rm tot}(V_0) - P_0 \Delta V + \frac{V_0}{2} \sum_{m,n-1}^{6} C_{mn} \varepsilon_m \varepsilon_n + O(\varepsilon_m^3) \tag{1}$$

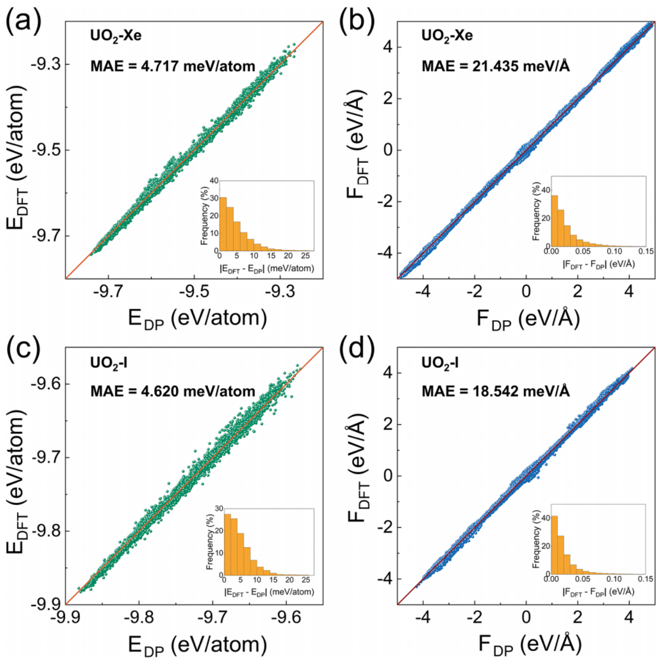

FIG. 1. Comparison of the energies and forces between the DFT and DP models over the structures sampled from the temperature range of 50 K to 1800 K: energies per atom of UO_2-Xe (a) and UO_2-I (c) systems; atomic forces of UO_2-Xe (b) and UO_2-I (d) systems. The insets show the distributions of the absolute errors, and the lines show the perfect correlations of the corresponding variables.

where V represents the volume of the lattice, while P_0 and V_0 denote the pressure and volume, respectively, of the undistorted system. Consequently, other mechanical properties, including bulk modulus, shear modulus, Young's modulus, and Poisson's ratio can be calculated by using the obtained elastic constants.

Finally, thermal conductivity was evaluated using the equilibrium molecular dynamics (EMD) method based on the Green-Kubo method [44,45]. The heat current autocorrelation function (HCACF) was integrated to calculate the thermal conductivity:

$$k = \frac{1}{3Vk_BT^2}\int_0^\infty \langle \vec{J}(t)\cdot\vec{J}(0)\rangle dt \tag{2}$$

where k is the thermal conductivity, t is the time, V is the system volume, T is the temperature, $\vec{J}(t)$ is the heat current at time t, and $\langle \vec{J}(t)\cdot\vec{J}(0)\rangle$ is the ensemble averaged HCACF [46].

III. RESULTS AND DISCUSSION

A. Verification of the DP model

The accuracy of our DP models was evaluated using validation datasets comprising over 3500 frames sampled from brief MD simulations in the DP-GEN procedure. Figure 1 compares the energies and forces between the DFT and DP models under different configurations. The insets of Fig. 1 highlight the mean absolute errors (MAE). For the UO_2-Xe system, the MAE for energy is 4.717 meV/atom [Fig. 1(a)], while the MAE for forces is 21.435 meV/Å [Fig. 1(b)]. Similarly, for the UO_2-I system, the MAE for energy is 4.620 meV/atom [Fig. 1(c)], while the MAE for forces is 18.542 meV/Å [Fig. 1(d)]. These results confirm that the trained DP models accurately predict both energy and forces for the UO_2-Xe and UO_2-I systems.

TABLE I. Comparison of UO_2 properties calculated from different potential functions with experimental results. The following properties were included: lattice constant a (Å), cohesion energy E_{coh} (eV/UO_2), and elastic constants C_{11}, C_{12}, C_{44} (GPa).

properties	DP_{U-O-Xe}	DP_{U-O-I}	Experiment [47–49]	Basak [50]	Morelon [51]	Cooper [52]
a	5.400	5.400	5.455	5.454[a]	5.447[a]	-
E_{coh}	–31.8	–31.2	–22.3	–43.2[a]	–65.9[a]	-
C_{11}	393.8	378.5	389.3	408.1[a]	216.9	406.3
C_{12}	129.4	120.8	118.7	61.2[a]	79.1	124.7
C_{44}	67.3	76.9	59.7	59.5[a]	78.5	63.9

[a]Reference [53]

Accurately predicting the ground-state structure is a fundamental capability of the DP models. Table I compares UO_2 properties calculated using different potential functions with experimental results. The lattice constant a of UO_2 was determined to be 5.400 Å by the DP models, in agreement with experiments (5.455 Å) and MD simulations using classical potentials (5.447 – 5.454 Å). Moreover, the cohesion energy E_{coh} was calculated as −31.8 eV/UO_2 for DP_{U-O-Xe} model and −31.2 eV/UO_2 for DP_{U-O-I} model. In comparison, the experimental cohesive energy is approximately −22.3 eV/UO_2, while MD simulation values range from −43.2 to −65.9 eV/UO_2. This indicates that our DP models deliver more accurate cohesive energy predictions, representing a significant improvement over classical potentials. Additionally, the elastic constants C_{11}, C_{12}, and C_{44} of UO_2 were calculated as 393.8 GPa, 129.4 Gpa, and 67.3 Gpa for the DP_{U-O-Xe} model, and 378.5 Gpa, 120.8 Gpa, and 76.9 GPa for the DP_{U-O-I} model. These calculated values closely match the experimental measurements (389.3 GPa, 118.7 GPa, and 59.7 GPa), and show significantly greater accuracy than predictions made using classical potentials (216.9–408.1 GPa, 61.2–124.7 GPa, and 59.5–78.5 GPa). These results demonstrate that our DP models exhibit excellent predictive accuracy for UO_2 properties, consistent with experimental results.

To apply DP models effectively in this study, it is crucial to assess the efficacy through defect formation energies. These energies indicate both the probability of defect formation and their stability. The detailed energy calculations in this section can be found in the Supplemental Material [54]. Table II compares our calculated formation energies of single vacancy and interstitial defects in UO_2 with DFT results and semi-empirical values. For U vacancies, the formation energies are 7.73 eV (DP_{U-O-Xe}) and 9.63 eV (DP_{U-O-I}), higher than those for O vacancies, which are 5.72 eV (DP_{U-O-Xe}) and 5.48 eV (DP_{U-O-I}). These values closely match the DFT results, indicating that vacancy defect formation requires substantial energy, making it less likely. Notably, the DP_{U-O-Xe} and DP_{U-O-I} models predict the formation energies of

TABLE II. Comparison of our calculated formation energies of single vacancy and interstitial defects (in eV) in UO_2 with those reported by other authors based on DFT and with semi-empirical values.

Defects	DP_{U-O-Xe}	DP_{U-O-I}	Iwasawa[a] [55]	Petit[a] [56]	Semi-empirical [57–60]
U vacancy	7.73	9.63	10.67	19.1	10.1–11.8
O vacancy	5.72	5.48	6.54	10.0	9.8–10.3
U interstitial	3.59	1.78	7.33	11.5	8.4–9.4
O interstitial	–2.55	–1.62	–0.15	–3.3	–5.5––4.5

[a]Based on DFT calculation.

3.59 eV and 1.78 eV for U interstitials, and −2.55 eV and −1.62 eV for O interstitials, respectively. The negative formation energies of O interstitials indicate that UO_2 is prone to oxidation in the presence of oxygen [55], in agreement with DFT and semi-empirical results (–5.5 eV to −0.15 eV). Furthermore, the formation energies for O vacancies and interstitials are lower than those of U, suggesting that observed defects are concentrated within the oxygen sublattice [56].

Additionally, it is crucial to assess the stability of FP at different pre-existing defect sites in UO_2. According to Brillant *et al.* [61], I prefers to occupy double vacancies, whereas Xe favors Schottky vacancies, both involving a single uranium vacancy. Therefore, this study evaluates the incorporation energies of FP by comparing the total energies of supercells with and without FP at U and O vacancies. Table III compares the incorporation energies of FP with previous results. For xenon, the incorporation energies in uranium and oxygen vacancies (Xe in V_U and Xe in V_O) are 4.51 eV and 7.89 eV, respectively. For iodine, the incorporation energies in uranium and oxygen vacancies (I in V_U and I in V_O) are 1.87 eV and 6.83 eV, respectively. These results are consistent with previous studies and indicate that Xe and I are more stable in uranium vacancies than in oxygen vacancies. Moreover, the higher incorporation energy for Xe compared to I suggests that Xe is more challenging to incorporate into UO_2.

Overall, these results confirm that the developed DP models accurately reproduce energies for the UO_2-Xe and UO_2-I systems, enabling atomic-scale insights into the structural stability and dynamic behavior of Xe and I within the UO_2 matrix over larger temporal and spatial scales with DFT-level precision.

B. Atomic diffusion and cluster formation of Xe and I in UO_2

Xe and I are typically volatile in the UO_2 matrix, resulting in rapid atomic diffusion. To investigate the effect of temperature on FP atomic diffusion in UO_2, a broad temperature range was explored (300–1700 K). The diffusion coefficients and energy barriers for FP diffusion in UO_2 were determined using the mean square displacement (MSD) method, offering an intuitive measure of the self-diffusion ability of FP atoms. The relationship between mean square displacement and time is given by the following equation:

$$\mathrm{MSD} = 6Dt + C \tag{3}$$

where D is the diffusion coefficient, and C is the initial displacement constant. Figure 2 illustrates the MSD of FP in UO_2-Xe and UO_2-I systems at different temperatures. As temperature increases, MSD rises correspondingly, suggesting faster FP diffusion. Notably, at the same temperature, the MSD of Xe [Fig. 2(a)] increases less than that of I [Fig. 2(b)], indicating that I diffuses more readily in UO_2 than Xe.

According to Eq. (3), the atomic diffusion coefficient is linearly related to MSD over sufficiently long periods, as expressed in the following equation:

$$D = \lim_{t\to\infty} \frac{1}{6t}\langle |r(t) - r(0)|^2\rangle \tag{4}$$

where $r(t)$ is the coordinate of the atom at time t, and $r(0)$ is its initial coordinate. Therefore, atomic diffusion coefficients can be derived from the slopes of MSD curves, independent of the time span. To minimize interference, the linear region of MSD curves, specifically between 20 and 80 ps, was chosen for analysis. Based on Eq. (4), diffusion coefficients of Xe and I at different temperatures were calculated.

In general, the diffusion coefficient follows the Arrhenius formula:

$$D = D_0 \exp\left(\frac{-E_a}{k_B T}\right) \tag{5}$$

where D_0 is the diffusion prefactor, E_a is the activation energy, k_B is the Boltzmann constant, and T is the temperature. Figure 3 presents the logarithm of FP diffusion coefficients as a function of the inverse temperature. Notably, the relationship between Ln(D) and 1/T is nonlinear across the whole temperature range for both Xe and I. This phenomenon has also been reported in previous studies [25,64,65]. These studies identified three distinct diffusion regimes: athermal, intermediate, and intrinsic. Our results similarly indicate distinct diffusion behaviors across low, intermediate, and high temperature regimes. Specifically, in our analysis, the temperature ranges for these regimes are: T ⩽ 800 K, 800 K < T ⩽ 1400

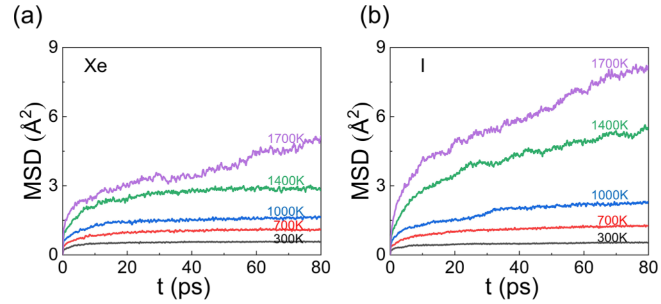

FIG. 2. Mean squared displacements of FP in UO_2-Xe (a) and UO_2-I (b) systems at 300 K, 700 K, 1000 K, 1400 K, and 1700 K.

TABLE III. Comparison of our calculated incorporation energies (in eV) of FP with previous results.

	DP_{U-O-Xe}	DP_{U-O-I}	Brillant [61]	Nerikar [62]	Jelea [63]
Xe in V_U	4.51		1.95	2.5	2.0–5.8
Xe in V_O	7.89		7.85	9.5	7.5–9.1
I in V_U		1.87	0.59		
I in V_O		6.83	2.55		

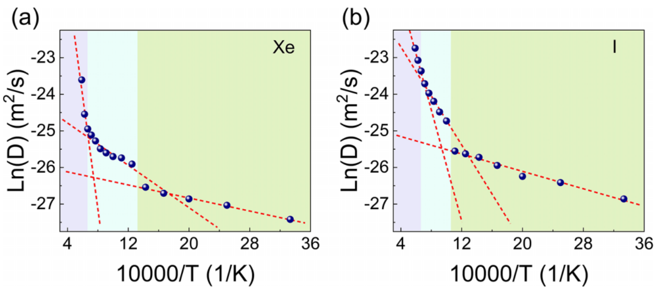

FIG. 3. Logarithm of diffusion coefficients of FP as a function of the inverse temperature in UO_2-Xe (a) and UO_2-I (b) systems. The temperature range is subdivided into three categories: a high-temperature zone, a medium-temperature zone, and a low-temperature zone. The lines show the linear fit between the corresponding variables.

K, and T > 1400 K for Xe, and T $\leqslant$ 1000 K, 1000 K < T $\leqslant$ 1400 K, and T > 1400 K for I. Notably, under identical concentration conditions, the Xe diffusion coefficients from the present study closely match the equation by Zamzamian *et al* [25]. For instance, the Xe diffusion coefficients at 700 K, 1200 K, and 1700 K (representing the three temperature regimes) are 2.97×10^{-12} m^2/s, 8.51×10^{-12} m^2/s and 5.59×10^{-12} m^2/s, respectively, compared to $\sim 2.32 \times 10^{-12}$ m^2/s, $\sim 10.1 \times 10^{-12}$ m^2/s and $\sim 5.24 \times 10^{-12}$ m^2/s derived from the equation [25]. Fitting the data across different temperature ranges yields Xe diffusion energy barriers of 0.04 eV, 0.12 eV, and 1.46 eV for low, intermediate, and high temperatures, respectively, closely matching the values of 0.05 eV, 0.17 eV, and ~1.30 eV shown in the reference illustrations [25]. Meanwhile, the I diffusion energy barriers are 0.05 eV, 0.31 eV, and 0.68 eV at low, intermediate, and high temperatures, respectively.

The rapid migration of insoluble FP atoms can lead to the formation of clusters, significantly affecting the microstructures of nuclear fuels. According to Zhang *et al.* [21], Xe bubbles form when the Xe concentration exceeds a certain threshold. Additionally, higher temperatures should accelerate FP atom migration and aggregation. To investigate the nucleation and growth of Xe and I clusters in UO_2, supercells containing $10 \times 10 \times 10$ UO_2 unit-cells were constructed by randomly removing 10% of UO_2 atoms and incorporating 5% Xe (UO_2-Xe system) or I atoms (UO_2-I system). MD simulations were conducted at 1400 K for 2000 ps, combined with Monte Carlo (MC) algorithms to simulate possible atomic swaps at intervals of 0.1 ps. Supplemental Figure S1 shows the potential energy variation in the UO_2-Xe and UO_2-I systems, initially decreasing and eventually reaching convergence [54].

Figure 4(a) illustrates the Xe atomic diffusion and cluster evolution prior to 700 ps. Initially, Xe atoms are uniformly distributed within the UO_2 matrix, with no clusters, leaving all atoms uncolored. By 100 ps, small Xe clusters begin to form and gradually grow as they incorporate additional Xe atoms. Between 200 and 300 ps, the largest cluster merges with the second-largest, significantly reducing the latter's size. In the later stages, clusters become larger and more distinct, with the largest cluster remaining fixed in a specific region. Figure 4(b) presents the sizes of the top five Xe clusters and their average size over 2000 ps. The cluster size is defined as the total number of FP atoms aggregated within a single cluster. The red curve, representing the second largest cluster, exhibits a sharp decline at 300 ps, corresponding to the cluster evolution in Fig. 4(a). The average cluster size gradually increases and eventually converges over time. By 700 ps, a super-large cluster containing over 300 Xe atoms forms and remains stable. Figure 4(c) tracks the number of clusters containing at least 2, 3, 4, or 5 Xe atoms, showing an overall decreasing trend as smaller clusters merge into larger ones.

Figure 4(d) presents the I atomic diffusion and cluster evolution. For I, the top five cluster sizes increase, with the largest cluster continuously changing position. Several large clusters containing dozens of I atoms are observed. Figure 4(e) shows the sizes of the top five I clusters and their average values. The sizes of I clusters increase gradually before stabilizing. Figure 4(f) indicates that the number of clusters containing at least 4 or 5 I atoms initially increases, followed by a decrease. These results highlight a significant difference in the self-attraction between Xe and I atoms.

In conclusion, Fig. 4 demonstrates the difference in cluster size and distribution between Xe and I aggregation behavior. Supplemental figure S2 shows the theoretically [54] calculated results about the potential energies of different configurations, *i.e.*, UO_2 incorporated dispersed FP atoms, small FP clusters, and large FP clusters, respectively [54]. The results demonstrate that Xe prefers to aggregate into large clusters rather than small ones, whereas I favor smaller clusters due to the lower potential energy of the configuration. Moreover, in the study by Brillant [61], the solution energies of Xe at uranium and oxygen vacancies (5.15 eV and 9.85 eV, respectively) are both higher than those of I (3.79 eV and 4.55 eV, respectively). This indicates that I atoms are more favorably incorporated into the UO_2 matrix, suggesting stronger interactions with the matrix compared to Xe. This is consistent with the expected behavior since Xe, as a noble gas, typically exhibits weak chemical interactions.

C. Effect of microstructural evolution on mechanical properties

During the migration and aggregation of Xe or I, the nuclear fuel undergoes microstructural evolution, leading to changes in its physical properties. Given the critical importance of mechanical properties for nuclear fuel safety, it is essential to assess how microstructural changes induced by FP migration impact the mechanical properties. Therefore, the mechanical properties, including elastic constants (C_{11}, C_{12}, and C_{44}), bulk modulus (B), shear modulus (G_H), Young's modulus (E), Poisson's ratio (ν), and volume expansion (V_t/V_0) were calculated for the UO_2-Xe and UO_2-I systems during FP atom migration and cluster growth (as shown in Fig. 4).

Figures 5(a), 5(b), and 5(c) show the changes in the elastic constants C_{11}, C_{12}, and C_{44} for the UO_2-Xe and UO_2-I systems during microstructural evolution. Notably, in the UO_2-Xe system, C_{11}, C_{12}, and C_{44} increase from 39.24 GPa, 16.94 GPa, and 7.99 GPa to their converged values of 81.38 GPa, 22.40 GPa, and 19.42 GPa, respectively. In contrast, in the

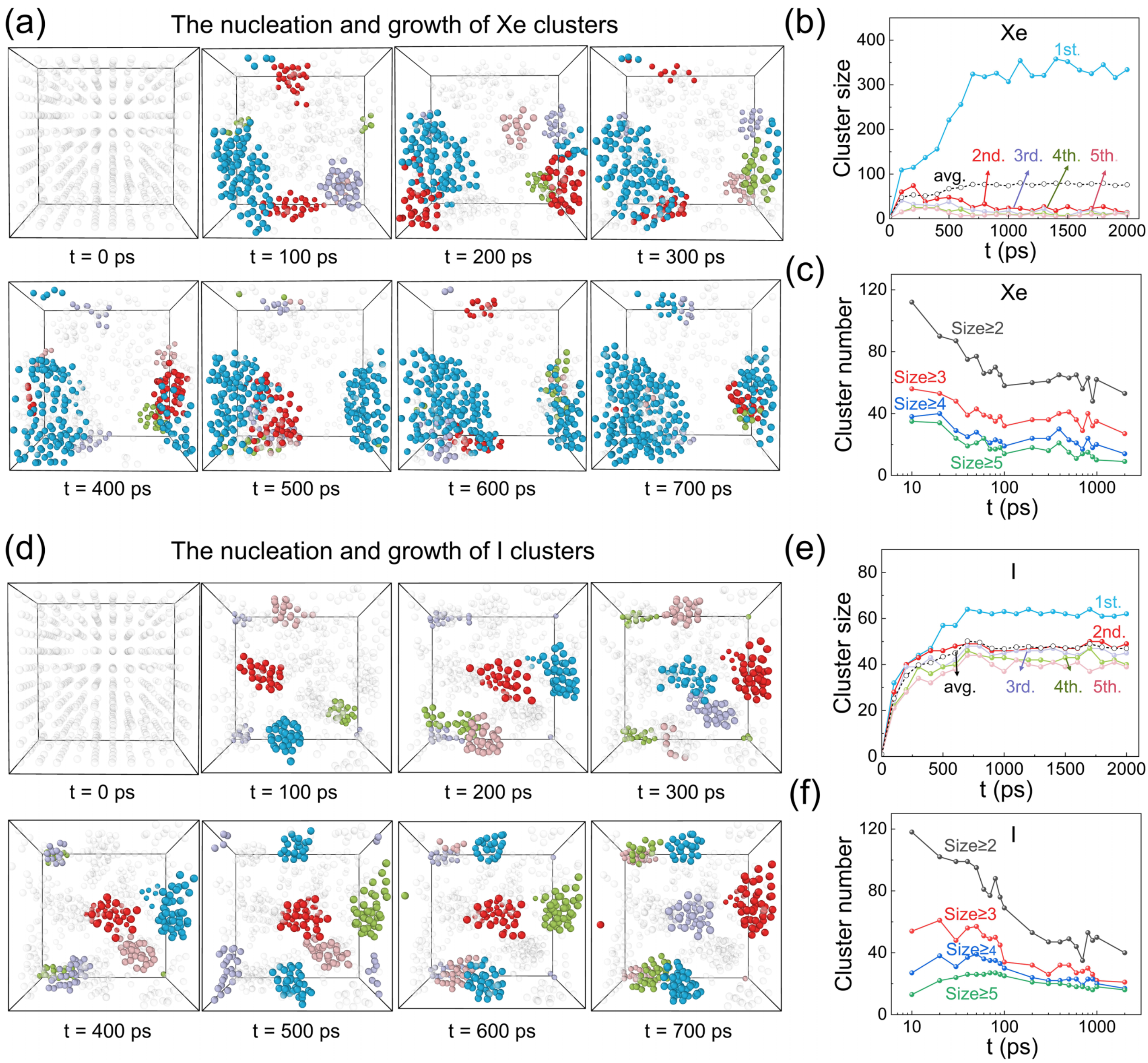

FIG. 4. FP atomic diffusion and cluster evolution in MD&MC simulations: the nucleation and growth of Xe (a) and I (d) clusters; cluster size of Xe (b) and I (e); cluster number of Xe (c) and I (f). In Figs. (a) and (d), the top five clusters are color-coded. In Figs. (b) and (e), the sizes of the top five clusters are shown, and their average values are calculated. In figures (c) and (f), the numbers of clusters containing at least 2, 3, 4, or 5 FP atoms are shown.

UO_2-I system, these elastic constants change from 84.24 GPa, 37.66 GPa, and 12.08 GPa to 182.00 GPa, 76.88 GPa, and 41.16 GPa, respectively. This trend indicates that the mechanical strength of the UO_2-Xe and UO_2-I fuels can be partially restored through the migration and aggregation of FP. Meanwhile, the elastic constants of the UO_2-Xe system are lower than those of the UO_2-I system at the same relaxation time and are significantly lower than those of pristine UO_2 (389.3 GPa, 118.7 GPa, and 59.7 GPa, as shown in Table I). These results demonstrate that FP atoms significantly reduce the elastic constants of UO_2, with Xe having a more pronounced effect than I.

Next, the bulk modulus B is calculated using the following equation:

$$B = \frac{C_{11} + 2C_{12}}{3} \tag{6}$$

Figure 5(d) presents the variation of the bulk modulus over relaxation time, following a trend similar to the elastic constants. For the UO_2-Xe system, B increases from 24.37 GPa to 42.06 GPa, while for the UO_2-I system, it rises from 53.19 GPa to 111.92 GPa, gradually converging over time. The bulk modulus nearly doubles following the migration and aggregation of FP.

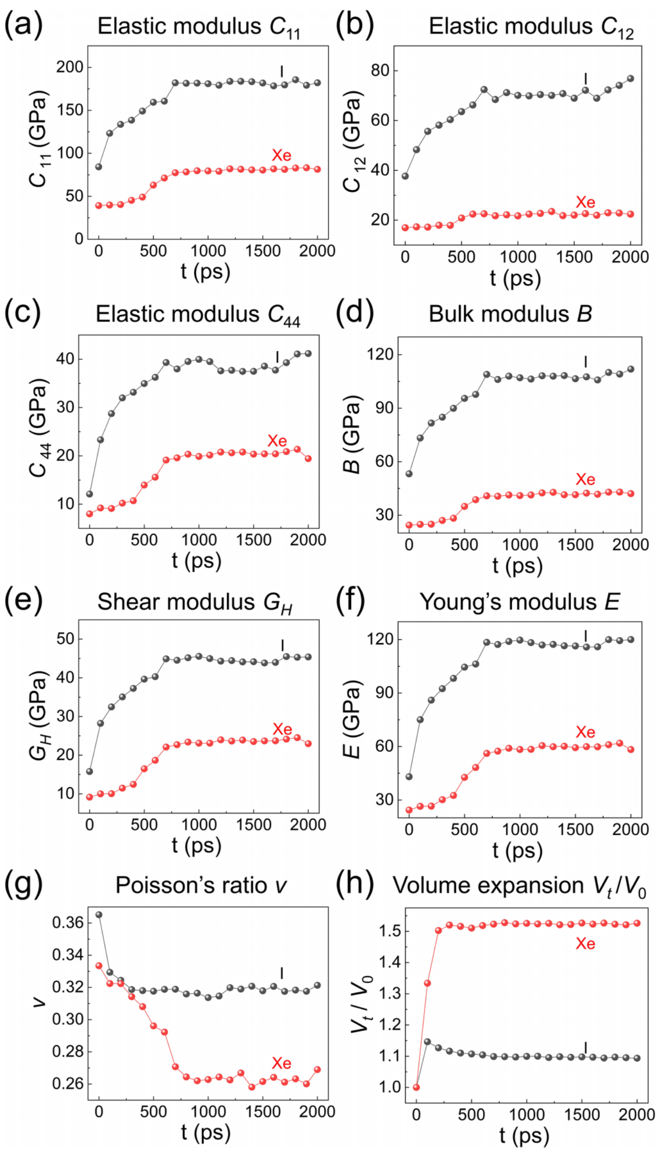

FIG. 5. Changes in the mechanical properties of UO_2-Xe and UO_2-I systems during microstructural evolution: (a) elastic modulus C_{11}; (b) elastic modulus C_{12}; (c) elastic modulus C_{44}; (d) bulk modulus B; (e) shear modulus G_H; (f) Young's modulus E; (g) Poisson's ratio ν; (h) volume expansion V_t/V_0.

The shear modulus is another essential mechanical property, measuring rigidity and resistance to reversible deformation under shear stress. Hill's method [66] is employed to calculate the shear modulus by first determining the Voigt shear modulus (G_V) and Reuss shear modulus (G_R) from elastic constants, using Eqs. (7) and (8) as below.

$$G_V = \frac{3C_{44} + C_{11} - C_{12}}{5} \tag{7}$$

$$G_R = \frac{5(C_{11} - C_{12})C_{44}}{4C_{44} + 3(C_{11} - C_{12})} \tag{8}$$

The Voigt and Reuss shear modulus represent the upper and lower bounds of the shear modulus, respectively [67]. The average of G_V and G_R, referred to as the Hill's shear modulus (G_H), is calculated using the following equation:

$$G_H = \frac{G_V + G_R}{2} \tag{9}$$

Figure 5(e) illustrates the calculated Hill's shear modulus, gradually increasing before converging. The converged values are 22.97 GPa for the UO_2-Xe system and 45.40 GPa for the UO_2-I system. The UO_2-Xe system exhibits relatively modest initial growth, with values consistently remaining lower than those of the UO_2-I throughout the corresponding timeframes. These results indicate that FP atomic diffusion and cluster growth enhance crystal rigidity. For pristine UO_2, the shear modulus G_H ranges from 88.54 GPa to 94.66 GPa (Supplemental Table S1), nearly four times higher than for UO_2-Xe and twice as high as for UO_2-I. This demonstrates that incorporating FP atoms significantly reduces the rigidity of UO_2 fuel.

Additionally, the Young's modulus E is derived from the bulk modulus and Hill's shear modulus using Eq. (10) [68]:

$$E = \frac{9BG_H}{3B + G_H} \tag{10}$$

Figure 5(f) shows the detailed results for E in the UO_2-Xe and UO_2-I systems. Although a gradual increase is observed, the final converged values of 58.30 GPa for UO_2-Xe and 119.97 GPa for UO_2-I remain significantly lower than those of pristine UO_2 (233.89–246.36 GPa, as shown in Supplemental Table S1 [54]). These findings indicate that the incorporation of FP markedly reduces UO_2 stiffness, diminishing its resistance to deformation. Notably, Xe cluster formation reduces the stiffness of UO_2 to nearly half the extent caused by I.

Additionally, the Poisson's ratio (υ) is calculated from the bulk modulus and Hill's shear modulus, according to Eq. (11):

$$\upsilon = \frac{3B - 2G_H}{2(3B + G)} \tag{11}$$

The results for Poisson's ratio are presented in Fig. 5(g). As expected, Poisson's ratio values are less than 0.5, aligning with the typical range. For pure UO_2, Poisson's ratio calculated using our DP models is 0.30–0.32 (Supplemental Table S1), consistent with the experimental value of 0.31 [69]. In the UO_2-Xe and UO_2-I systems, Poisson's ratio initially exceeds that of pure UO_2 but gradually decreases and stabilizes. For the UO_2-Xe system, it converges to 0.26 from an initial value of 0.33, while for the UO_2-I system, it decreases from 0.37 to a final value of 0.32. This trend indicates that FP cluster growth reduces the fuel's ability to undergo transverse shrinkage during tensile deformation.

Finally, FP clusters cause fuel swelling, resulting in internal stress in the nuclear fuel and potential safety risks. Figure 5(h) illustrates the volume expansions of the UO_2-Xe and UO_2-I systems during the migration and aggregation of FP. The lattice volume increases significantly as FP atoms diffuse and form clusters, eventually stabilizing within a specific range. In the UO_2-Xe system, the equilibrium volume expansion reaches 1.5 times the initial volume, compared to 1.1 times in the UO_2-I system. These results demonstrate that Xe atomic diffusion and cluster growth cause significantly larger volume expansion in UO_2 than I, potentially increasing the risk to nuclear power security.

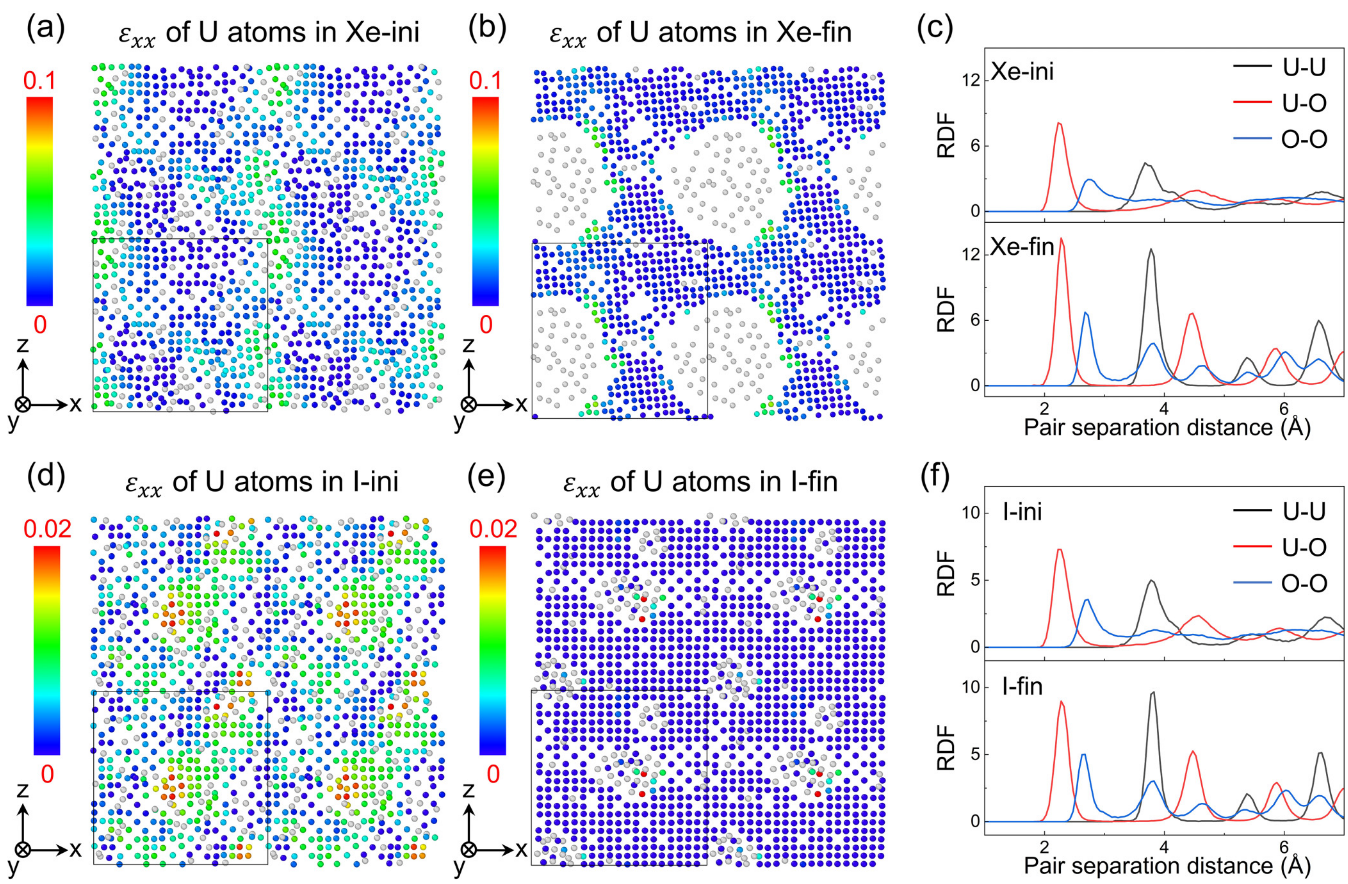

FIG. 6. Strain tensor component ε_{xx} of U atoms and radial distribution functions in UO_2-Xe and UO_2-I systems under 500 MPa: (a) ε_{xx} of U atoms in UO_2-Xe initial system; (b) ε_{xx} of U atoms in UO_2-Xe final system; (c) RDF of UO_2-Xe systems; (d) ε_{xx} of U atoms in UO_2-I initial system; (e) ε_{xx} of U atoms in UO_2-I final system; (f) RDF of UO_2-I systems. In (a), (b), (d), and (e), the gray atoms are FP atoms, and the oxygen atoms are not displayed.

To gain deeper insight into the changes in mechanical properties, an in-depth investigation of the atomic-scale evolution of the UO_2-Xe and UO_2-I systems was performed. A uniaxial tensile stress of 500 MPa was applied along the x-axis to both the initial (Xe-ini and I-ini) and final (Xe-fin and I-fin) configurations of the UO_2-Xe and UO_2-I systems. The initial configurations show a dispersed distribution of FP atoms, while the final configurations feature large FP clusters. Then, the atomic strain tensor for each atom was derived using atomic displacement vectors and the atomic deformation gradient tensor, based on the initial and final atomic positions [70,71]. To enhance visualization, one $x - z$ slice was extracted, and a $2x \times 2z$ supercell extension was generated for display. Additionally, the radial distribution functions (RDF) for these configurations were calculated.

Figure 6(a) shows the strain tensor component ε_{xx} for U atoms in Xe-ini. Statistical analysis reveals that 59.6% of the atomic strain values exceeded 0.01, and 28.1% surpassed 0.02. In contrast, in Fig. 6(b), the ε_{xx} for U atoms in Xe-fin is less pronounced than in Xe-ini [Fig. 6(a)], with significant strain observed only at the interfaces between Xe clusters and the UO_2 matrix. The analysis further indicates that 26.5% of the atomic strain values exceed 0.01, and 10.1% exceed 0.02, both less than half of the values in Xe-ini. This suggests that the UO_2-Xe system transitions from a "soft" material into a "tough" material after the migration and aggregation of Xe, with only the Xe clusters and their interfaces with the UO_2 matrix retaining softness. Figure 6(c) shows the RDF curves for Xe-ini and Xe-fin. In Xe-ini, UO_2 matrix exhibits a distinct peak at short pair separation distances, while broader and lower peaks emerge as the pair separation distance increases, indicating the less-crystalline (even amorphous) nature of the disordered atomic arrangement. After Xe atoms aggregate into large clusters, the crystalline characteristics of the matrix become more pronounced. Compared to Xe-ini, the peaks for U-U, U-O, and O-O in Xe-fin are significantly sharper and higher, indicating a more compact and crystalline matrix structure. This structural difference is a key factor contributing to the difference in strain conditions between Xe-ini and Xe-fin.

Figures 6(d) and 6(e) illustrate the strain tensor components for U atoms in the I-ini and I-fin configurations, respectively. Similar to the UO_2-Xe system [Figs. 6(a) and 6(b)], the atomic strain in I-ini is more pronounced than in I-fin. However, for the UO_2-I system, the maximum atomic strain is only 0.023, significantly smaller than the 0.074 in the UO_2-Xe system. This indicates that UO_2-I is a tougher material than UO_2-Xe. Additionally, Fig. 6(f) presents the RDF curves for the I-ini and I-fin. Compared to I-ini, the crystalline features in I-fin are more prominent. Notably, the peak heights

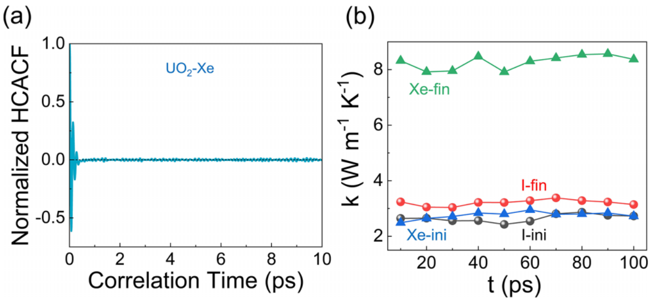

FIG. 7. (a) The heat current autocorrelation function for UO_2-Xe system at 300 K. (b) The thermal conductivities k for the initial and final configurations of UO_2-Xe and UO_2-I systems.

for U-U, U-O, and O-O in I-fin are significantly lower than those in Xe-fin, indicating that the UO_2 matrix in I-fin is less compact and crystalline than that in Xe-fin. These findings are consistent with the observations in Fig. 4, which show many smaller I clusters that are more sparsely distributed within the UO_2 matrix in the UO_2-I system compared to the UO_2-Xe system.

The above results indicate that the effects of FP atoms are localized, suggesting that the interaction between FP atoms and UO_2 matrix atoms is much weaker than that between matrix atoms themselves. Accordingly, the scattered FP atoms in the initial configuration lead to a relatively relaxed and soft lattice structure. However, after the migration and aggregation of FP, the UO_2 matrix becomes more closely packed, resulting in a denser and tougher lattice structure. This microstructural evolution also explains the changes in the mechanical properties discussed earlier. These insights are valuable for improving nuclear fuel safety and extending operational lifespans by deepening our understanding of FP atomic diffusion and cluster growth.

D. Effect of microstructural evolution on thermal conductivity

Besides mechanical properties, thermal conductivity is a critical factor affecting energy conversion efficiency and fuel system safety. Investigating how the migration and aggregation of FP and corresponding microstructural changes influence thermal conductivity of UO_2 is essential. In this study, the Green-Kubo method, a widely used approach in MD simulations [72–75], was employed to evaluate the thermal conductivity of UO_2-based fuel. To validate our DP models for thermal conductivity calculations, MD simulations were performed on pure UO_2. Our DP models predict the thermal conductivity of UO_2 to be $14.85\,\mathrm{W\,m^{-1}\,K^{-1}}$ at 300 K, consistent with previous MD simulation results ($\sim 14 - 16\,\mathrm{W\,m^{-1}\,K^{-1}}$) reported by others [75–77], as shown in Supplemental Table S2. These results confirm the accuracy of our DP models in predicting thermal conductivity.

Figure 7(a) shows the heat current autocorrelation function (HCACF) for the UO_2-Xe system at 300 K, and Supplemental Figure S3 shows the HCACF for UO_2-I system and pure UO_2 [54]. The HCACF converges within 10 ps, validating the choice of correlation time. All simulations were performed for 100 ps using the NVE ensemble, with thermal conductivity calculated at 10 ps intervals. Figure 7(b) presents the thermal conductivities for the initial and final configurations of UO_2-Xe and UO_2-I systems. The average thermal conductivities are 2.76 and $8.28\,\mathrm{W\,m^{-1}\,K^{-1}}$ for Xe-ini and Xe-fin, and 2.65 and $3.21\,\mathrm{W\,m^{-1}\,K^{-1}}$ for I-ini and I-fin, all of which are lower than the thermal conductivity of pure UO_2. The thermal conductivity of Xe-ini is approximately equivalent to that of I-ini. However, after the migration and aggregation of FP, the thermal conductivity of UO_2-Xe improves nearly threefold compared to its initial state, while the thermal conductivity of UO_2-I increases by only about 20%. It demonstrates that the effect of microstructural change on the thermal conductivity is much more significant in the UO_2-Xe system than in the UO_2-I system.

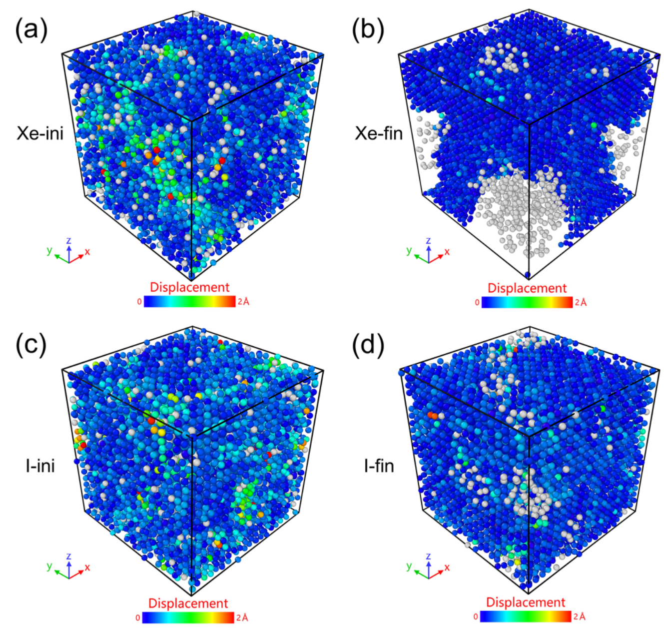

FIG. 8. In the calculation of thermal conductivity, the atomic displacement of each U and O atom in the Xe-ini (a), Xe-fin (b), I-ini (c), and I-fin (d) configurations. The gray atoms are FP atoms.

In crystalline materials, phonons, as the quantized energy of lattice vibration, are responsible for heat conduction. Theoretically, FP atoms within the UO_2 lattice disrupt its periodicity and crystal symmetry, creating numerous discrete phonon scattering centers that significantly reduce thermal conductivity [78,79]. To investigate lattice vibration, the average displacements of each U and O atom relative to their equilibrium positions were determined for both the initial and final configurations, as shown in Fig. 8. Figures 8(a) and 8(b) reveal that the atomic displacements in the Xe-ini are significantly greater than those in Xe-fin. The results indicate that dispersed FP atoms cause substantial distortion in phonon vibration patterns, disturbing energy and momentum distribution. This distortion leads to intense phonon-FP atom scattering, frequent directional changes, and a reduction in thermal conductivity. Therefore, the thermal conductivity of the UO_2 system with dispersed FP atoms is significantly lower than that of pure UO_2. This finding is consistent with the study from Liu [78], which demonstrates that even a low concentration of Xe (0.34%) significantly reduces thermal conductivity, demonstrating the considerable impact of dispersed FP atoms on phonon scattering by altering vibration wave properties. After the migration and aggregation of Xe atoms into clusters, only a few interfacial atoms surrounding the Xe clusters exhibit substantial vibrations. It indicates that when FP atoms form clusters, phonon scattering primarily occurs at the cluster surface and nearby regions. Thus, less dispersed Xe atoms within the UO_2 matrix decrease phonon scattering centers, resulting in the improvement of thermal conductivity. Similarly, Figs. 8(c) and 8(d) demonstrate that the atomic displacements in I-ini are much greater than in I-fin. The thermal conductivity of the UO_2-I system also improves after the migration and aggregation of I.

Notably, in comparison to dispersed FP atoms within the UO_2 matrix, Xe aggregation enhances thermal conductivity by nearly threefold, while I aggregation only yields a 20% increase. This difference can be attributed to reduced phonon scattering resulting from fewer residual dispersed Xe atoms remaining in UO_2. After the migration and aggregation of FP atoms, the fraction of residual FP atoms within the UO_2 matrix is 21.5% (129 I atoms) for I-fin and 11% (66 Xe atoms) for Xe-fin. Therefore, fewer dispersed Xe atoms within UO_2 lead to less frequent phonon scattering, significantly improving the thermal conductivity compared to the UO_2-I system.

IV. CONCLUSIONS

In summary, the atomic migration and aggregation of Xe and I in UO_2 were investigated and compared through MD simulations using deep potential (DP) models. The accuracy and generalization capabilities of the DP models were thoroughly validated. MD simulation results revealed that the mean square displacement (MSD) of FP increases with rising temperature, with I exhibiting higher diffusion capacity than Xe at any specific temperature. Consistent with previous studies, three distinct temperature-dependent diffusion behaviors were identified. In combined MD and Monte Carlo (MD&MC) simulations, FP atoms were observed to aggregate into clusters with varying distributions. Xe atoms formed a distinctly larger cluster containing over 300 atoms, whereas I atoms formed several medium-sized clusters, each consisting of tens of atoms. Further analysis demonstrated that the incorporation of FP reduces the mechanical properties and thermal conductivity of UO_2. Notably, the aggregation of FP atoms into clusters partially restores these physical properties. Xe clustering results in a more pronounced reduction in mechanical properties but enables a greater recovery of thermal conductivity compared to I clustering. The changes in mechanical properties were attributed to atomic strain and alterations in the crystalline structure of the UO_2 matrix, while variations in thermal conductivity were explained by examining atomic displacements within the matrix. These findings provide valuable insights into the effects of FP migration and aggregation on UO_2 fuel properties, offering guidance for improving fuel performance and reactor safety.

ACKNOWLEDGMENTS

This study is financially supported by the Innovative Scientific Program of CNNC. The authors gratefully acknowledge the support from the Fund of Science and Technology on Reactor Fuel and Materials Laboratory (Grant No. STRFML-2022–15). The authors also thank F. Yang and X. Zhang at the Network Information Center of Xi'an Jiaotong University for supporting the HPC platform.

DATA AVAILABILITY

The data that support the findings of this article are not publicly available. The data are available from the authors upon reasonable request.

[1] J. Rest, A model for the effect of the progression of irradiation-induced recrystallization from initiation to completion on swelling of UO_2 and U–10Mo nuclear fuels, J. Nucl. Mater. **346**, 226 (2005).
[2] H. Xiao, Modeling of fission gas swelling in LWR UO_2 fuel under irradiation, Prog. Nucl. Energy **90**, 122 (2016).
[3] T. Winter and C. Deo, Comparison of fission gas swelling models for amorphous U_3Si_2 and crystalline UO_2, Ann. Nucl. Energy **100**, 31 (2017).
[4] G. Brillant, Interpretation and modelling of fission product Ba and Mo releases from fuel, J. Nucl. Mater. **397**, 40 (2010).
[5] G. Brillant, C. Marchetto, and W. Plumecocq, Ruthenium release from fuel in accident conditions, Radiochim. Acta **98**, 267 (2010).
[6] M. Adamson and S. Vaidyanathan, Mechanistic models for cesium thermomigration and cesium-fuel chemomechanical interactions in mixed-oxide fuel-pins, Trans. Am. Nucl. Soc. (United States) **38**, CONF-810606- (1981)..
[7] I. Johnson and C. Johnson, Mass-spectrometry studies of fission product behavior: I. Fission products released from irradiated LWR fuel, J. Nucl. Mater. **154**, 67 (1988).
[8] B. Cox, Pellet clad interaction (PCL) failures of zirconium alloy fuel cladding - A review, J. Nucl. Mater. **172**, 249 (1990).
[9] H. Kleykamp, The solubility of selected fission products in UO_2 and (U, Pu)O_2, J. Nucl. Mater. **206**, 82 (1993).
[10] M. H. A. Piro, D. Sunderland, S. Livingstone, J. Sercombe, R. W. Revie, A. Quastel, K. A. Terrani, and C. Judge, *Pellet-Clad Interaction Behavior in Zirconium Alloy Fuel Cladding*, Comprehensive Nuclear Materials (Elsevier, Amsterdam, 2020), pp. 248–306.
[11] C. G. Doll, C. M. Sorensen, T. W. Bowyer, J. I. Friese, J. C. Hayes, E. Hoffmann, and R. Kephart, Abatement of xenon and iodine emissions from medical isotope production facilities, J. Environ. Radioact. **130**, 33 (2014).
[12] W. R. Schell, M. J. Tobin, D. J. Marsan, C. W. Schell, J. Vives-Batlle, and S. R. Yoon, Measurement of fission product gases in the atmosphere, Nucl. Instrum. Meth. A **385**, 277 (1997).
[13] X.-Y. Liu and D. A. Andersson, Molecular dynamics study of fission gas bubble nucleation in UO_2, J. Nucl. Mater. **462**, 8 (2015).
[14] Y. Yun, H. Kim, H. Kim, and K. Park, Atomic diffusion mechanism of Xe in UO_2, J. Nucl. Mater. **378**, 40 (2008).

[15] W. H. Hocking, D. W. Shoesmith, and J. S. Betteridge, Reactivity effects in the oxidative dissolution of UO_2 nuclear fuel, J. Nucl. Mater. **190**, 36 (1992).
[16] A. C. S. Sabioni, W. B. Ferraz, and F. Millot, First study of uranium self-diffusion in UO_2 by SIMS, J. Nucl. Mater. **257**, 180 (1998).
[17] H. Matzke, Atomic transport properties in UO_2 and mixed oxides $(U, Pu)O_2$, J. Chem. Soc. Faraday Trans. 2 **83**, 1121 (1987).
[18] A. C. S. Sabioni, W. B. Ferraz, and F. Millot, Effect of grain boundaries on uranium and oxygen diffusion in polycrystalline UO_2, J. Nucl. Mater. **278**, 364 (2000).
[19] P. Lösönen, On the behaviour of intragranular fission gas in UO_2 fuel, J. Nucl. Mater. **280**, 56 (2000).
[20] G. Sattonnay, L. Vincent, F. Garrido, and L. Thomé, Xenon versus helium behavior in UO_2 single crystals: A TEM investigation, J. Nucl. Mater. **355**, 131 (2006).
[21] W. Zhang, D. Yun, and W. Liu, Xenon diffusion mechanism and xenon bubble nucleation and growth behaviors in molybdenum via molecular dynamics simulations, Materials **12**, 2354 (2019).
[22] E. Moore, L. René Corrales, T. Desai, and R. Devanathan, Molecular dynamics simulation of Xe bubble nucleation in nanocrystalline UO_2 nuclear fuel, J. Nucl. Mater. **419**, 140 (2011).
[23] M. W. D. Cooper, S. T. Murphy, M. J. D. Rushton, and R. W. Grimes, Thermophysical properties and oxygen transport in the $(U_x, Pu_{1-x})O_2$ lattice, J. Nucl. Mater. **461**, 206 (2015).
[24] L. Wang, Z. Wang, Y. Xia, Y. Chen, Z. Liu, Q. Wang, L. Wu, W. Hu, and H. Deng, Effects of point defects on the stable occupation, diffusion and nucleation of Xe and Kr in UO_2, Metals **12**, 789 (2022).
[25] S. M. Zamzamian, A. Zolfaghari, and Z. Kowsar, Molecular dynamics investigation of xenon, uranium, and oxygen diffusion in UO_2 nuclear fuel, Comput. Mater. Sci. **211**, 111553 (2022).
[26] X. Zhu, H. Gong, Y.-F. Zhao, D.-Y. Lin, G. Han, T. Liu, and H. Song, Effect of Xe bubbles on the thermal conductivity of UO_2: Mechanisms and model establishment, J. Nucl. Mater. **533**, 152080 (2020).
[27] H. Wang, L. Zhang, J. Han, and W. E, DeePMD-kit: A deep learning package for many-body potential energy representation and molecular dynamics, Comput. Phys. Commun. **228**, 178 (2018).
[28] L. Zhang, J. Han, H. Wang, R. Car, and W. E, Deep potential molecular dynamics: A scalable model with the accuracy of quantum mechanics, Phys. Rev. Lett. **120**, 143001 (2018).
[29] J. Wu, L. Bai, J. Huang, L. Ma, J. Liu, and S. Liu, Accurate force field of two-dimensional ferroelectrics from deep learning, Phys. Rev. B **104**, 174107 (2021).
[30] R. He, H. Wu, L. Zhang, X. Wang, F. Fu, S. Liu, and Z. Zhong, Structural phase transitions in $SrTiO_3$ from deep potential molecular dynamics, Phys. Rev. B **105**, 064104 (2022).
[31] Z. Gong, J. Z. Liu, X. Ding, J. Sun, and J. Deng, Strain-aided room-temperature second-order ferroelectric phase transition in monolayer PbTe: Deep potential molecular dynamics simulations, Phys. Rev. B **108**, 134112 (2023).
[32] Z. Gong, J. Z. Liu, X. Ding, J. Sun, and J. Deng, Strain-induced two-dimensional relaxor ferroelectrics in Se-doped PbTe, Phys. Rev. B **109**, 054117 (2024).
[33] T. Wen, L. Zhang, H. Wang, W. E, and D. J. Srolovitz, Deep potentials for materials science, Mater. Futures **1**, 022601 (2022).
[34] Y. Zhang, H. Wang, W. Chen, J. Zeng, L. Zhang, H. Wang, and W. E, DP-GEN: A concurrent learning platform for the generation of reliable deep learning based potential energy models, Comput. Phys. Commun. **253**, 107206 (2020).
[35] P. Hohenberg and W. Kohn, Inhomogeneous Electron Gas, Phys. Rev. **136**, B864 (1964).
[36] W. Kohn and L. J. Sham, Self-consistent equations including exchange and correlation effects, Phys. Rev. **140**, A1133 (1965).
[37] P. E. Blöchl, Projector augmented-wave method, Phys. Rev. B **50**, 17953 (1994).
[38] G. Kresse and D. Joubert, From ultrasoft pseudopotentials to the projector augmented-wave method, Phys. Rev. B **59**, 1758 (1999).
[39] J. P. Perdew, K. Burke, and M. Ernzerhof, Generalized gradient approximation made simple, Phys. Rev. Lett. **77**, 3865 (1996).
[40] S. Plimpton, Fast parallel algorithms for short-range molecular dynamics, J. Comput. Phys. **117**, 1 (1995).
[41] M. Parrinello and A. Rahman, Polymorphic transitions in single crystals: A new molecular dynamics method, J. Appl. Phys. **52**, 7182 (1981).
[42] S. Nosé, A unified formulation of the constant temperature molecular dynamics methods, J. Chem. Phys. **81**, 511 (1984).
[43] A. Stukowski, Visualization and analysis of atomistic simulation data with OVITO–the open visualization tool, Modelling Simul. Mater. Sci. Eng. **18**, 015012 (2010).
[44] M. S. Green, Markoff random processes and the statistical mechanics of time-dependent phenomena. II. Irreversible processes in fluids, J. Chem. Phys. **22**, 398 (1954).
[45] R. Kubo, Statistical-mechanical theory of irreversible processes. I. General theory and simple applications to magnetic and conduction problems, J. Phys. Soc. Jpn. **12**, 570 (1957).
[46] J. Kang and L.-W. Wang, First-principles Green-Kubo method for thermal conductivity calculations, Phys. Rev. B **96**, 020302 (2017).
[47] M. T. Hutchings, High-temperature studies of UO_2 and ThO_2 using neutron scattering techniques, J. Chem. Soc. Faraday Trans. 2 **83**, 1083 (1987).
[48] M. S. S. Brooks and P. J. Kelly, On the cohesive energy and charge density of uranium dioxide, Solid State Commun. **45**, 689 (1983).
[49] A. Padel and Ch. De Novion, Constantes elastiques des carbures, nitrures et oxydes d'uranium et de plutonium, J. Nucl. Mater. **33**, 40 (1969).
[50] C. B. Basak, A. K. Sengupta, and H. S. Kamath, Classical molecular dynamics simulation of UO_2 to predict thermophysical properties, J. Alloys Compd. **360**, 210 (2003).
[51] N.-D. Morelon, D. Ghaleb, J.-M. Delaye, and L. Van Brutzel, A new empirical potential for simulating the formation of defects and their mobility in uranium dioxide, Philos. Mag. **83**, 1533 (2003).
[52] M. W. D. Cooper, M. J. D. Rushton, and R. W. Grimes, A many-body potential approach to modelling the thermomechanical properties of actinide oxides, J. Phys. Condens. Matter **26**, 105401 (2014).
[53] K. Govers, S. Lemehov, M. Hou, and M. Verwerft, Comparison of interatomic potentials for UO_2. Part I: Static calculations, J. Nucl. Mater. **366**, 161 (2007).

[54] See Supplemental Material at http://link.aps.org/supplemental/10.1103/f3kx-84sy for detailed computational methods, including the calculations of defect formation and incorporation energies, potential energies of various systems and configurations, heat current autocorrelation functions, properties of UO_2 predicted by DP models, and comparisons between DP models and other computational approaches.

[55] M. Iwasawa, Y. Chen, Y. Kaneta, T. Ohnuma, H.-Y. Geng, and M. Kinoshita, First-principles calculation of point defects in uranium dioxide, Mater. Trans. **47**, 2651 (2006).

[56] T. Petit, C. Lemaignan, F. Jollet, B. Bigot, and A. Pasturel, Point defects in uranium dioxide, Philos. Mag. B **77**, 779 (1998).

[57] R. A. Jackson, A. D. Murray, J. H. Harding, and C. R. A. Catlow, The calculation of defect parameters in UO_2, Philos. Mag. A **53**, 27 (1986).

[58] S. Nicoll, Hj. Matzke, and C. R. A. Catlow, A computational study of the effect of Xe concentration on the behaviour of single Xe atoms in UO_2, J. Nucl. Mater. **226**, 51 (1995).

[59] C. R. A. Catlow, Point defect and electronic properties of uranium dioxide, Proc. R. Soc. Lond. A **353**, 533 (1977).

[60] C. R. A. Catlow, Fission gas diffusion in uranium dioxide, Proc. R. Soc. Lond. A **364**, 473 (1978).

[61] G. Brillant, F. Gupta, and A. Pasturel, Fission products stability in uranium dioxide, J. Nucl. Mater. **412**, 170 (2011).

[62] P. V. Nerikar, X.-Y. Liu, B. P. Uberuaga, C. R. Stanek, S. R. Phillpot, and S. B. Sinnott, Thermodynamics of fission products in $UO_{2\pm x}$, J. Phys. Condens. Matter **21**, 435602 (2009).

[63] A. Jelea, R. J.-M. Pellenq, and F. Ribeiro, An atomistic modeling of the xenon bubble behavior in the UO_2 matrix, J. Nucl. Mater. **444**, 153 (2014).

[64] J. A. Turnbull, C. A. Friskney, J. R. Findlay, F. A. Johnson, and A. J. Walter, The diffusion coefficients of gaseous and volatile species during the irradiation of uranium dioxide, J. Nucl. Mater. **107**, 168 (1982).

[65] C. Matthews, R. Perriot, M. W. D. Cooper, C. R. Stanek, and D. A. Andersson, Cluster dynamics simulation of xenon diffusion during irradiation in UO_2, J. Nucl. Mater. **540**, 152326 (2020).

[66] L. Zuo, M. Humbert, and C. Esling, Elastic properties of polycrystals in the Voigt-Reuss-Hill approximation, J. Appl. Crystallogr. **25**, 751 (1992).

[67] T. Vazhappilly and A. Kumar Pathak, Effect of lanthanide fission product concentrations on the mechanical properties of UO_2: A *first principle* based study, Comput. Theor. Chem. **1209**, 113610 (2022).

[68] M. Sanati, R. C. Albers, T. Lookman, and A. Saxena, Elastic constants, phonon density of states, and thermal properties of UO_2, Phys. Rev. B **84**, 014116 (2011).

[69] J. B. Wachtman, M. L. Wheat, H. J. Anderson, and J. L. Bates, Elastic constants of single crystal UO_2 at 25 °C, J. Nucl. Mater. **16**, 39 (1965).

[70] M. L. Falk and J. S. Langer, Dynamics of viscoplastic deformation in amorphous solids, Phys. Rev. E **57**, 7192 (1998).

[71] F. Shimizu, S. Ogata, and J. Li, Theory of shear banding in metallic glasses and molecular dynamics calculations, Mater. Trans. **48**, 2923 (2007).

[72] T. Arima, S. Yamasaki, Y. Inagaki, and K. Idemitsu, Evaluation of thermal properties of UO_2 and PuO_2 by equilibrium molecular dynamics simulations from 300 to 2000K, J. Alloys Compd. **400**, 43 (2005).

[73] S. Nichenko and D. Staicu, Molecular Dynamics study of the mixed oxide fuel thermal conductivity, J. Nucl. Mater. **439**, 93 (2013).

[74] S. Nichenko and D. Staicu, Molecular Dynamics study of the effects of non-stoichiometry and oxygen Frenkel pairs on the thermal conductivity of uranium dioxide, J. Nucl. Mater. **433**, 297 (2013).

[75] C. I. Maxwell and J. Pencer, Molecular dynamics modelling of the thermal conductivity of off-stoichiometric $UO_{2\pm x}$ and $(U_yPu_{1-y})O_{2\pm x}$ using equilibrium molecular dynamics, Ann. Nucl. Energy **131**, 317 (2019).

[76] R. Brandt and G. Neuer, Thermal conductivity and thermal radiation properties of UO_2, J. Non-Equilib. Thermodyn. **1**, 3 (1976).

[77] P. B. Weisensee, J. P. Feser, and D. G. Cahill, Effect of ion irradiation on the thermal conductivity of UO_2 and U_3O_8 epitaxial layers, J. Nucl. Mater. **443**, 212 (2013).

[78] X.-Y. Liu, M. W. D. Cooper, K. J. McClellan, J. C. Lashley, D. D. Byler, B. D. C. Bell, R. W. Grimes, C. R. Stanek, and D. A. Andersson, Molecular dynamics simulation of thermal transport in UO_2 containing uranium, oxygen, and fission-product defects, Phys. Rev. Appl. **6**, 044015 (2016).

[79] W. Chen, M. W. D. Cooper, Z. Xiao, D. A. Andersson, and X.-M. Bai, Effect of Xe bubble size and pressure on the thermal conductivity of UO_2—A molecular dynamics study, J. Mater. Res. **34**, 2295 (2019).